Controlling $4f$ antiferromagnetic dynamics via itinerant electronic susceptibility

Sang-Eun Lee ⬤,[1,2,*] Yoav William Windsor ⬤,[1] Daniela Zahn ⬤,[1] Alexej Kraiker ⬤,[3] Kurt Kummer ⬤,[4] Kristin Kliemt ⬤,[3]
Cornelius Krellner ⬤,[3] Christian Schüßler-Langeheine ⬤,[5] Niko Pontius ⬤,[5] Urs Staub ⬤,[6] Denis V. Vyalikh ⬤,[7,8]
Arthur Ernst ⬤,[9,10,†] and Laurenz Rettig ⬤[1,‡]

[1]*Department of Physical Chemistry, Fritz-Haber-Institut der Max-Planck-Gesellschaft, Faradayweg 4-6, 14195 Berlin, Germany*
[2]*Center of Integrated Nanotechnologies, Los Alamos National Laboratory, Los Alamos, New Mexico 87545, USA*
[3]*Physikalisches Institut, Goethe-Universität Frankfurt, Max-von-Laue-Strasse 1, 60438 Frankfurt am Main, Germany*
[4]*European Synchrotron Radiation Facility, BP 220, F-38043 Grenoble Cedex, France*
[5]*Helmholtz-Zentrum Berlin für Materialien und Energie GmbH, Albert-Einstein-Strasse 15, 12489 Berlin, Germany*
[6]*Swiss Light Source, Paul Scherrer Institut, Forschungsstrasse 111, 5232 Villigen PSI, Switzerland*
[7]*Donostia International Physics Center (DIPC), Paseo Manuel de Lardizabal 4, 20018 Donostia/San Sebastián, Basque Country, Spain*
[8]*IKERBASQUE, Basque Foundation for Science, Plaza Euskadi 5, 48009 Bilbao, Spain*
[9]*Institute for Theoretical Physics, Johannes Kepler University, Altenberger Strasse 69, 4040 Linz, Austria*
[10]*Max-Planck-Institut für Mikrostrukturphysik, Weinberg 2, 06120 Halle (Saale), Germany*

Optical manipulation of magnetism holds promise for future ultrafast spintronics, especially with lanthanides and their huge, localized $4f$ magnetic moments. These $4f$ moments interact indirectly by spin polarizing the conduction electrons (the Ruderman-Kittel-Kasuya-Yosida exchange interaction), influenced by interatomic orbital overlap, and the conduction electron's susceptibility around the Fermi level. Here, we study this influence in a series of $4f$ antiferromagnets, GdT_2Si$_2$ (T = Co, Rh, Ir), using ultrafast resonant x-ray diffraction. We observe a twofold increase in the ultrafast intersublattice angular momentum transfer rate between the materials, originating from modifications in the conduction electron susceptibility, as confirmed by first-principles calculations.

I. INTRODUCTION

Lanthanides are becoming increasingly important in technology due to their exceptionally large magnetic moments. Since the majority of the magnetic moments of lanthanides resides in spatially localized $4f$ electron shells [1,2], magnetic moments from different lanthanide atoms can only interact indirectly by spin-polarizing itinerant conduction electrons that surround the $4f$ moments. This indirect interaction is called the Rudermann-Kittel-Kasuya-Yosida (RKKY) exchange interaction [3]. As its mechanism implies, not only the localized $4f$ moments but also the itinerant conduction electrons play an important role in determining the strength of the RKKY interaction J_{RKKY} in lanthanide-based magnetic materials. J_{RKKY} is proportional to the squared overlap integral between the $4f$ and conduction electrons, $|I|^2$, and the susceptibility χ of the

conduction electrons' spin polarization around the Fermi level to an effective magnetic field formed by $4f$ magnetic moments ($J_{RKKY} \propto |I|^2 \chi$) [3].

The ultrafast dynamics of magnetic devices after femtosecond laser excitation is governed by the transfer speed of angular momentum between its microscopic subsystems. While the investigation of such ultrafast spin dynamics has been employed to study these interactions for several decades [4,5], and also numerous studies of lanthanide magnetism have been reported [6–14], the influence of the individual contributions of J_{RKKY} to ultrafast spin dynamics has remained mostly elusive. In particular, whereas the role of the localized $4f$ magnetic moments has been extensively studied mostly in the heavy trivalent lanthanides (Gd-Tm) [6,12,13], the role of the itinerant conduction electrons in lanthanide magnetism has not been systematically investigated so far since many elemental lanthanides share very similar conduction electron structures, making it difficult to isolate their specific role in ultrafast magnetization dynamics. However, due to their central role in the RKKY interaction, a systematic investigation of the influence of the conduction electron properties on the magnetization dynamics in lanthanide-based compounds is of strong interest.

For this purpose, we investigated the ultrafast magnetization dynamics in a series of $4f$ antiferromagnetic (AF) compounds LnT_2Si$_2$ [Ln: lanthanides; T: transition metals; see Fig. 1(a)], which share almost identical magnetic and

*Contact author: sang-eun@lanl.gov
†Contact author: arthur.ernst@jku.at
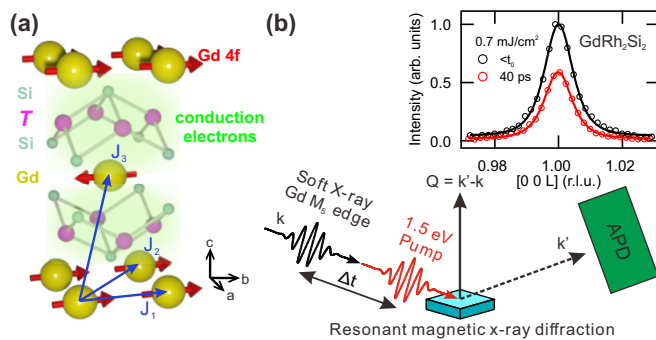‡Contact author: rettig@fhi-berlin.mpg.de

FIG. 1. (a) Crystal structure of GdT_2Si_2 (T = Co, Rh, and Ir). J_1, J_2 are exchange coupling between the nearest and the next-nearest in-plane *4f* moments, and J_3 is the exchange coupling between the nearest out-of-plane *4f* moments. (b) Sketch of the experimental setup. Top: Pump-induced suppression of the (001) magnetic diffraction peak of $GdRh_2Si_2$.

lattice structures [15,16]. Using this similarity, we recently investigated the role of the *4f* moments on the ultrafast spin dynamics of $LnRh_2Si_2$ by varying the lanthanide *Ln* [14], which demonstrated that the direct spin transfer between antiferromagnetically coupled *4f* moments is an essential demagnetization channel during ultrafast spin dynamics scaling with the strength of the RKKY interaction. In this study, in a similar approach we systematically vary the nonmagnetic transition metal *T* occupation within GdT_2Si_2 from *3d* to *5d* (Co, Rh, Ir), and single out the influence on the RKKY interaction and the ultrafast spin dynamics in these *4f* antiferromagnets. Surprisingly, we find a nonmonotonous variation of angular momentum transfer rates with *d*-shell occupation, with $GdRh_2Si_2$ showing larger transfer rates than the other two compounds. Using *ab initio* calculations, we explain this behavior by the variation of the conduction electron susceptibility χ due to a competition of the *T*-ion *d*-orbital extension and the *d*-level energy splitting.

II. METHODS

A. Experiments

The family of intermetallics GdT_2Si_2 (T = Co *3d*, Rh *4d*, and Ir *5d*) crystallizes in the tetragonal $ThCr_2Si_2$ structure (a = $b \sim 4$ Å, $c \sim 10$ Å) and are A-type antiferromagnets, where antiferromagnetically ordered Gd ions are separated by T_2Si_2 blocks along the c axis [Fig. 1(a)] [16,17]. The sample growth condition and characterization are elaborated in Appendix A. The Néel temperatures T_N of the three samples are 45 K (Co), 107 K (Rh), and 85 K (Ir) [11,18]. In GdT_2Si_2, the magnetic moments are carried by the seven unpaired Gd *4f* electrons, while the conduction electrons including the *T* states are only indirectly spin polarized [15,19].

Employing resonant soft x-ray diffraction (RXD), we measured the resonantly enhanced [0 0 L] magnetic diffraction intensity, sensitive to long-range AF ordering of Gd *4f* moments along the c axis [Fig. 1(b)]. The samples were characterized at the RESOXS end station of the SIM beam line of the Swiss Light Source at the Paul Scherrer Institute, Switzerland, and the RIXS end station of the ID32 beam line

of the European Synchrotron Radiation Facility in Grenoble, France [20,21]. Time-resolved resonant soft x-ray diffraction (trRXD) experiments were performed at the FemtoSpeX beam line UE56/1-ZPM of BESSY II of the Helmholtz-Zentrum Berlin, Germany, which uses femtosecond slicing to provide ultrashort soft x-ray pulses [22]. We used 50-fs-long laser pulses centered at 1.55 eV, at a repetition rate of 3 kHz, to excite the sample and measured the transient diffraction intensity of 100-fs-long sliced soft x-ray pulses centered at the Gd M_5 absorption edge at $\sim$1188 eV with an avalanche photodiode (APD), at a repetition rate of 6 kHz [Fig. 1(b)]. All dynamical experiments were conducted at a temperature of 20 K.

B. First-principles calculations

First-principles calculations were carried out using a self-consistent Green's function method [23,24] within the density functional theory in a generalized gradient approximation (GGA) [25]. Strongly localized Gd *4f* electronic state were treated within a GGA+U method applying $U = 6.0$ eV [26]. Exchange constants were obtained utilizing the magnetic force theorem, implemented within the multiple scattering theory [27]. Critical temperatures were estimated within a random phase approximation [28].

III. RESULTS AND DISCUSSION

A. Characterization of antiferromagnetic GdT_2Si_2

While $GdIr_2Si_2$ shows a commensurate magnetic diffraction peak at constant $L = 1$ at all temperatures [Fig. 2(a)] similar to $GdRh_2Si_2$ [11], $GdCo_2Si_2$ displays incommensurate magnetic diffraction peaks at $L = q$ and $2 - q$ with $q \sim 0.966$ at 20 K, which shift with temperature [Fig. 2(b)]. Since the two incommensurate peaks exhibit an almost identical temperature and photon-energy dependence, we concentrate on the (0 0 q) peak in this study.

The magnetic diffraction intensity of the three samples exhibits almost identical temperature dependencies following a mean-field-like behavior (Gd, $S = 7/2$) [Fig. 2(c)]. The similar photon-energy dependence of resonant enhancement at the Gd M_5 absorption edge ($h\nu \sim 1188$ eV; *3d* $\rightarrow$ *4f*) demonstrates their similar orbital and magnetic configuration [Fig. 2(d)], and leads to very similar penetration depths of $\sim$4 nm at resonance, corresponding to the x-ray light probing $\sim$4 unit cells of GdT_2Si_2 [11,14,29]. These similarities in both temperature and photon-energy dependence demonstrate their similar long-range *4f* antiferromagnetism, justifying the following comparative analysis of ultrafast spin dynamics.

B. Ultrafast dynamics of long-range *4f* antiferromagnetic order in GdT_2Si_2

The femtosecond dynamics of the AF order parameter, given by the square-root of the (0 0 L) magnetic diffraction peak amplitude are shown for selected fluences in Fig. 3(a). The dynamics at all measured pump fluences discussed in this study are presented in Appendix B. In the case of $GdRh_2Si_2$, the peak amplitudes have been separated from a transient reorientation of the magnetic in-plane
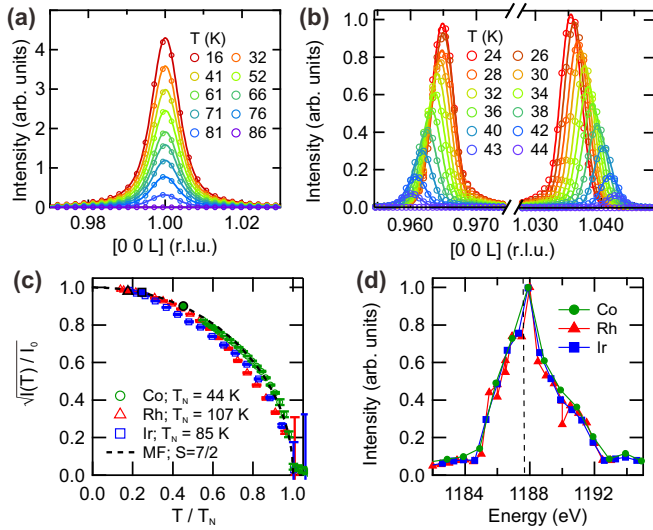
FIG. 2. Temperature-dependent behavior of the magnetic diffraction intensity of (a) GdIr$_2$Si$_2$ and (b) GdCo$_2$Si$_2$. (c) Equilibrium temperature-dependent behavior of the magnetic diffraction amplitude of GdT_2Si$_2$ (symbols). The dashed line is a mean-field curve for $S = 7/2$ corresponding to Gd [1]. Bold solid symbols indicate the estimated staggered magnetization of each sample at 20 K, the base temperature of the dynamic measurements. (d) Photon-energy-dependent resonant amplification of the magnetic diffraction intensity of GdT_2Si$_2$ (symbols). The vertical dashed line indicates the photon energy that we chose for the rest of this study (1187.5 eV).

easy axis using a procedure that combines several azimuthal orientations [11]. To account for pump-induced transient peak shifts, the peak amplitudes for GdCo$_2$Si$_2$ have been corrected by considering the transient peak position evolution of the (0 0 *L*) diffraction peak, as detailed in Appendix C.

For a quantitative comparison of the demagnetization dynamics of the three materials, we modeled the demagnetization curves using a phenomenological exponential decaying functions describing different timescales,

$$A(t) = 1 - \Theta(t, t_0) \sum_i^{f,s} A_i(1 - e^{-(t-t_0)/\tau_i}), \qquad (1)$$

where A_f, A_s, and τ_f, τ_s are the amplitude and the time constant of the fast (~ 1 ps) and slow (~ 30–100 ps) processes, respectively. t_0 corresponds to the temporal overlap of pump and probe pulses, and $\Theta(t, t_0)$ is the Heaviside function. The observed demagnetization timescales of the three compounds are comparable with the dynamics in other antiferro- and ferromagnetic 4*f* compounds [6,10,14].

Figure 3(b) presents the demagnetization amplitude $\Delta m = A_f + A_s$ as functions of fluence normalized to the critical fluence F_C, defined for each material as the fluence necessary to induce 50% demagnetization [14] (Details of the absorbed fluence estimation are provided in Appendix D.) We find values for F_C of 0.60 (Co), 1.74 (Rh), and 1.36 (Ir) mJ/cm^2, respectively, which surprisingly do not follow the *d*-shell occupation of the *T* ions, but instead show a linear relationship to T_N [inset of Fig. 3(b)]. A similar relation with a comparable slope has also been observed in LnRh$_2$Si$_2$ (Ln=Pr-Ho) [14]. This scaling relation between the critical fluence F_C and the Néel
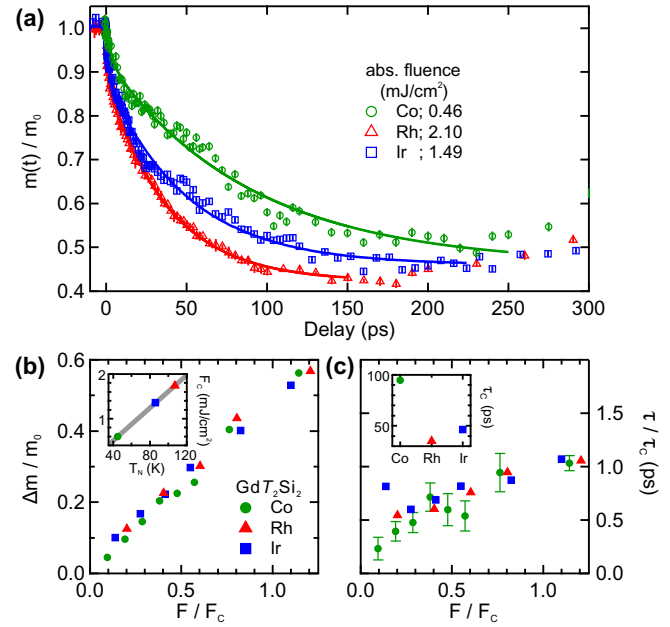

FIG. 3. (a) Ultrafast dynamics of the normalized (0 0 *L*) magnetic diffraction amplitude of GdT_2Si$_2$ (T = Co, Rh, and Ir) at a selected pump fluence acquired at a constant momentum transfer Q. Error bars denote uncertainties from Poisson statistics. Solid lines are exponential decaying functions for phenomenological description (see text). (b) Demagnetization amplitude of the three samples plotted along the fluence F normalized by the critical fluence F_C (see text) of each sample. Inset: The relation between the critical fluence and the Néel temperature of each sample. (c) Normalized slow demagnetization time constants τ/τ_C of the three samples plotted along the normalized fluence F/F_C. Inset: Time constants τ_C at the critical fluence used for normalization.

temperature T_N implies that the relevant magnetic interactions follow a classical mean-field-like behavior [14], supporting the validity of our comparative analysis of the ultrafast spin dynamics of GdT_2Si$_2$.

The normalized time constants of the slow demagnetization process τ_s, which is present in all materials, are shown in Fig. 3(c). They exhibit a qualitatively similar square-root-like behavior with F/F_C, albeit the absolute timescales differ substantially [see the inset of Fig. 3(c)], similar to our previous study [14]. Thus, while all of the studied materials exhibit qualitatively similar demagnetization behavior, there are also notable differences. Whereas GdRh$_2$Si$_2$ and GdIr$_2$Si$_2$ display a two-step decay in their demagnetization dynamics ($\tau_f \sim 1$ ps, $\tau_s > 10$ ps), followed by a slow recovery after ~ 100 ps, τ_f is almost absent in GdCo$_2$Si$_2$. Furthermore, similar to the critical fluences, we find substantial differences in the demagnetization rate, following the same sequence (GdRh$_2$Si$_2$ and GdCo$_2$Si$_2$ exhibiting the fastest and the slowest dynamics, respectively).

For accurate comparison of the demagnetization rates, the ultrafast angular momentum transfer rate $\alpha = m_{stag}\mu_{4f}A_s/\tau_s$ is calculated for each material [14], where $\mu_{4f}=7\mu_B$ is the size of the Gd *4f* moments [3]. The staggered magnetization m_{stag} of each sample at 20 K is indicated in Fig. 1(c) with bold solid markers. The fluence-dependent behavior of the
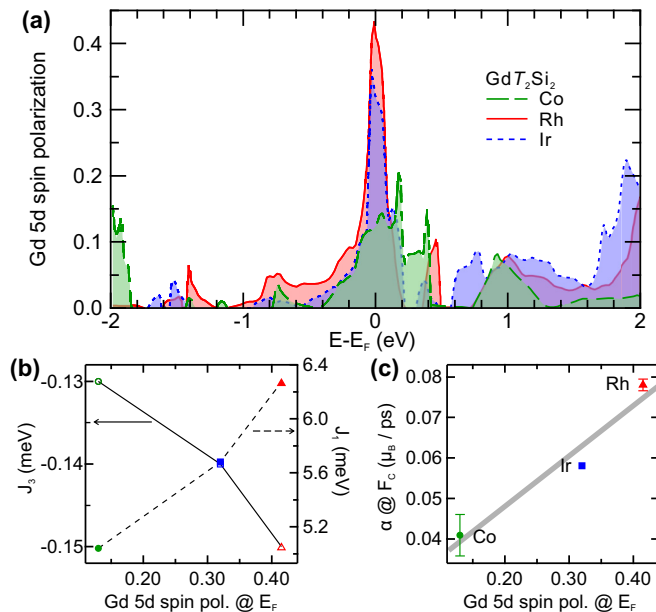
FIG. 4. (a) Energy distribution of calculated spin polarization of Gd *5d* states of GdT_2Si$_2$ in the vicinity of the Fermi level E_F. (b) Calculated indirect RKKY exchange interaction between the nearest in-plane *4f* moments J_1 (closed markers, dashed line, right axis) and the nearest out-of-plane antiferromagnetically coupled *4f* moments J_3 (open markers, solid line, left axis) plotted along the calculated Gd *5d* spin polarization. (c) Angular momentum transfer rate at F_C interpolated from fluence dependence (see Appendix B) plotted along the Gd *5d* spin polarization of the three samples. The gray line is a guide to the eyes. Error bars are derived from error propagation of the demagnetization time constant and amplitude of each compound.

angular momentum transfer rates is shown in Appendix B. Similarly to the inverse time constants and critical fluences, GdRh$_2$Si$_2$ (*4d*) has the largest α, followed by GdIr$_2$Si$_2$ (*5d*) and GdCo$_2$Si$_2$ (*3d*). Although they share the same Gd *4f* moments, the angular momentum transfer rate of the GdT_2Si$_2$ series varies by ∼100% (Fig 4(c)).

C. Scaling of the angular momentum transfer rate with Gd *5d* spin polarization around the Fermi level

In order to understand the reason for the varying ultrafast angular momentum transfer rate of the GdT_2Si$_2$ series, we calculated exchange coupling constants and electronic densities of states (eDOS) of GdT_2Si$_2$ employing density functional theory (DFT) (see Sec. II B for details). According to the DFT calculations, in GdT_2Si$_2$, the conduction electrons are mostly composed of *5d* electrons. Thus, the interaction between the local magnetic moments is mediated predominantly via spin-polarized Gd *5d* states. As discussed in Sec. I, the strength of the RKKY interaction J_{RKKY} is determined by the overlap integral between *4f* and conduction electrons and the nonlocal susceptibility of the conduction electrons' spin polarization around the Fermi level E_F. Since all the studied compounds share the same local magnetic moments and Gd *5d* electrons, the overlap integral factor does not vary much among the GdT_2Si$_2$ series.

In contrast, the calculations show that the spin polarization of Gd *5d* electrons around E_F, i.e., the difference in eDOS of majority- and minority-spin states, varies substantially between the different compounds [Fig. 4(a)]. At the Fermi level, GdRh$_2$Si$_2$ has the largest spin polarization, followed by GdIr$_2$Si$_2$ and GdCo$_2$Si$_2$. As shown in Fig. 4(b), the spin polarization at E_F also directly correlates with the strength of the calculated RKKY interaction between the nearest in-plane and out-of-plane Gd *4f* moments [J_1, J_3, respectively, in Fig. 1(a)]. This varying spin polarization implies that the transition metal ions modify the eDOS of both majority- and minority-spin states and thus the nonlocal susceptibility of the conduction electrons' spin polarization in the vicinity of the Fermi level. At the same time, we also find a clear scaling relation of the experimental angular momentum transfer rate with the Gd *5d* spin polarization at E_F [Fig. 4(c)]. As shown for the LnRh$_2$Si$_2$ series [14], the ultrafast angular momentum transfer rate in this series of compounds scales with the strength of the RKKY interaction. Therefore, the observed scaling relation with the Gd *5d* spin polarization [Fig. 4(c)] reflects the influence of the conduction electrons' susceptibility on the ultrafast spin dynamics of the GdT_2Si$_2$ series due to varying nonmagnetic T ions.

Besides the antiferromagnetic interplane coupling J_3, the in-plane coupling constants J_1, which are responsible for establishing in-plane ferromagnetic order, also vary among the series [Fig. 4(b)]. Among the antiferromagnetic LnT_2Si$_2$ compounds, GdT_2Si$_2$ exhibit the strongest intersublattice angular momentum transfer between the antiparallel Gd *4f* spins [14]. Thus, phonon-mediated Elliott-Yafet spin-flip scattering processes within the planes due to J_1 are expected to contribute only weakly. Therefore, even though the in-plane exchange couplings vary with the T ions, the general conclusion that we yield from the antiferromagnetic dynamics does not change substantially.

D. Two competing factors affecting the Gd *5d* spin polarization around E_F

The behavior of the *5d* electrons in GdT_2Si$_2$ explored in our calculations can be explained by two important factors. The first important factor is the extension of the transition metal wave functions. These orbitals show an increasing degree of delocalization when going from the *3d* to the *5d* shell, with GdCo$_2$Si$_2$ showing the strongest localization (see the regions highlighted in magenta in Fig. 5). Therefore, the hybridization between the Si and Co states is much weaker than the hybridization between the Si and Ir/Rh states in GdIr$_2$Si$_2$ and GdRh$_2$Si$_2$. Consequently, with increasing delocalization of T d orbitals along the series, the vacant Si valence electrons hybridize less with the Gd *5d* states, increasing the *5d* eDOS and hence the spin polarization at the Fermi level [Fig. 6(a)]. The second factor influencing the *5d* DOS is the bonding/antibonding splitting of T d states, and their distance to E_F. Here, the distance of the antibonding states from E_F increases from Co to Ir (see the regions highlighted in yellow in Fig. 5), leading to a reduction of the eDOS near E_F along the series [Fig. 6(b)], which in consequence decreases the spin polarization near E_F as well. Combined with the first factor,
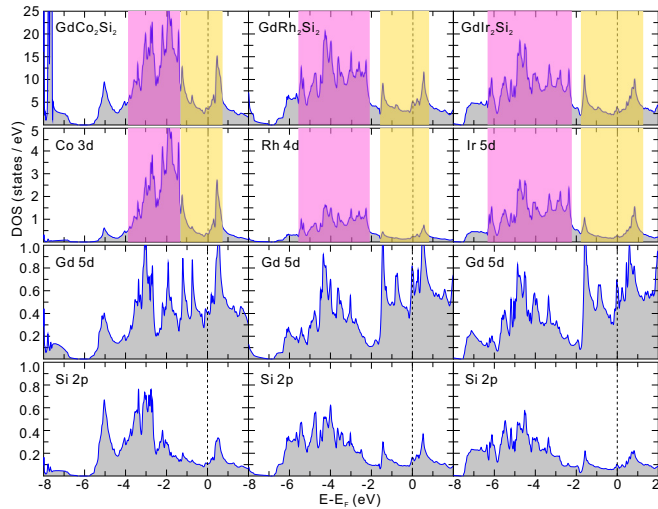
FIG. 5. Total and element-resolved densities of states (DOS) of GdT_2Si_2: $T=$ Co (left panel), Rh (middle), Ir (right panel). In the element-resolved DOS, only the most important orbital contributions are shown. The shaded area in the total and transition metal (T) d-orbital DOS highlights localization of T d-wave functions (magenta) and splitting of the bonding and antibonding states around the Fermi level (yellow), which are discussed in the main text.

this explains the observed behavior of the largest eDOS and angular momentum transfer in $GdRh_2Si_2$ [Fig. 6(c)].

In addition, the particular crystalline structure of GdT_2Si_2 supports this trend. As shown in Ref. [30], the magnetic properties of the lanthanide compounds are highly sensitive
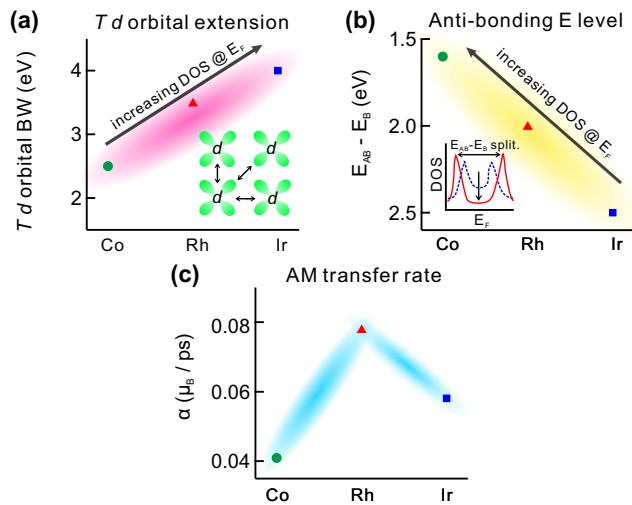

FIG. 6. Cartoon summarizing the factors contributing to the scaling of the ultrafast angular momentum transfer rate of GdT_2Si_2 with respect to the transition metal (T) ions, $3d$ Co, $4d$ Rh, and $5d$ Ir. (a) The extension of T d orbitals is reflected by their calculated bandwidth (Fig. 5, purple areas). (b) The distance between the bonding/antibonding orbitals with respect to the Fermi level is reflected by the energy splitting of the calculated unoccupied antibonding T d and occupied T d states (Fig. 5, yellow areas). (c) The combined effect of the trends in (a) and (b) leads to the observed behavior of spin susceptibility and angular momentum transfer rates.

to changes in unit cell volumes: a reduction of the unit cell volume leads to a reduction of $5d$ eDOS at the Fermi level, thereby modifying the magnetic interaction in the system. In our case, the variation of the unit cell volume ($GdCo_2Si_2$: 150.0 Å^3 [17] < $GdIr_2Si_2$: 156.0 Å^3 [16] < $GdRh_2Si_2$: 162.9 Å^3 [15]) reflects the changes in eDOS and spin polarization at E_F.

Finally, a comparison to semimetallic ferromagnets appears interesting. While, in these systems, enhanced spin polarization accompanied by reduced band overlap and DOS results in decreased demagnetization rates by blocking either phonon-mediated spin-flip scattering or diffusive spin transport [31–33], our study found the opposite behavior for antiferromagnetic intersublattice angular momentum transfer due to enhanced RKKY coupling for larger DOS and spin polarization. This observation underlines the importance of RKKY-driven intersublattice angular momentum transfer for the ultrafast spin dynamics in these $4f$ antiferromagnetic systems.

IV. CONCLUSIONS

In summary, we investigated the role of the itinerant conduction electrons in ultrafast spin dynamics of $4f$ antiferromagnets. By substituting the T ions in GdT_2Si_2 ($T=$ Co, Rh, Ir), we selectively modified their conduction electron susceptibility and measured the femtosecond dynamics of magnetic diffraction intensity at various pump fluences employing time-resolved resonant magnetic soft x-ray diffraction. While we found qualitatively similar demagnetization behavior upon optical excitation at 1.55 eV, the observed critical fluences and ultrafast angular momentum transfer rates α vary drastically, and nonmonotonously with T orbital shell (α: $GdRh_2Si_2$ > $GdIr_2Si_2$ > $GdCo_2Si_2$). First-principles calculations of the electronic density of states and exchange coupling constants of GdT_2Si_2 employing density functional theory show that the spin polarization of Gd $5d$ electrons scales with the in-plane and out-of-plane nearest-neighbor exchange coupling constants, and with the experimental angular momentum transfer rate. This implies that varying the T ions modifies the non-local susceptibility of conduction electrons' spin polarization and, hence, the strength of the RKKY interaction. We explain this effect by a combination of d-orbital wave-function localization and bonding/antibonding splitting of T d states, modifying the electronic density of states around the Fermi level and their nonlocal susceptibility. Our findings provide important insights for designing lanthanide-based magnetic devices, showing how a modification of the itinerant conduction electrons, which could, e.g., be implemented by chemical or electrostatic doping, impacts ultrafast angular momentum transfer processes.

The data that support the findings of this article are openly available [34].

ACKNOWLEDGMENTS

APPENDIX A: SAMPLE GROWTH AND CHARACTERIZATION

The GdRh$_2$Si$_2$ and GdIr$_2$Si$_2$ single crystals were obtained according to the procedure described earlier [15,16]. For the growth of GdCo$_2$Si$_2$ single crystals, high-purity starting materials were weighed in a graphite crucible and sealed in a niobium crucible under argon atmosphere. The stoichiometric mixture of the elements was used with the ratio 1 : 2 : 2 : 24 (Gd : Co : Si : In) with indium as flux. The growth was performed as described in Ref. [16] with a maximum temperature of the furnace of 1550 °C.

Powder x-ray diffraction yielded lattice parameters of $a = b = 3.911$ Å and $c = 9.803$ Å, which are in good agreement with the literature [35]. Energy dispersive x-ray spectroscopy (EDX) revealed the stoichiometry of Gd : Co : Si $= 20 \pm 1$: 39 ± 2 : 41 ± 2, which is in good agreement with the 122 target stoichiometry within the experimental error. The orientation of the single crystals was determined using the Laue method.

APPENDIX B: ULTRAFAST ANTIFERROMAGNETIC ORDER DYNAMICS OF Gd*T*$_2$Si$_2$

Ultrafast long-range *4f* sublattice magnetization dynamics of Gd*T*$_2$Si$_2$ (*T* = Co, Rh, Ir) at various pump fluences are presented in Figs. 7(a)–7(c). Curves presented in Fig. 2 of the main text are selected from this set of demagnetization curves in Fig. 7. As discussed in the main text, note that the demagnetization dynamics of GdCo$_2$Si$_2$ are corrected for a
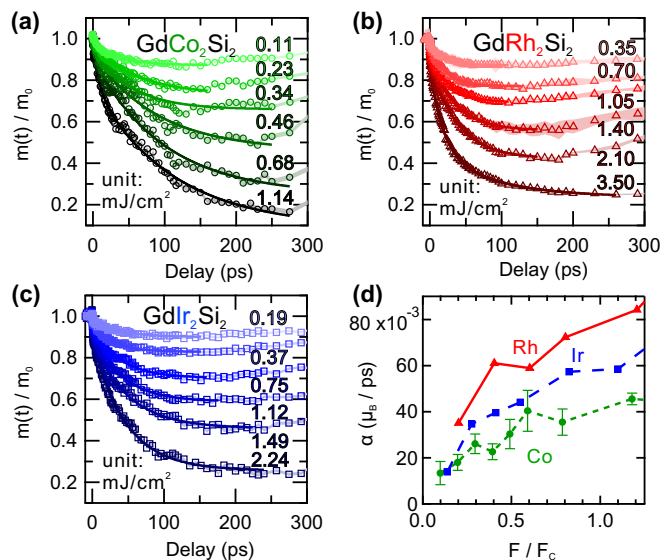

FIG. 7. (a)–(c) Ultrafast antiferromagnetic order dynamics of Gd*T*$_2$Si$_2$ (*T*= Co, Rh, Ir) at various pump fluences. Solid lines are a phenomenological description of the decaying part of the curves using exponentially decaying functions (see main text). Numbers along with each curve indicate the absorbed fluence. (d) Ultrafast angular momentum transfer of Gd*T*$_2$Si$_2$ plotted along the normalized fluence (fluence divided by the critical fluence of each material; see main text).

possible transient magnetic diffraction peak shift, which is detailed in Appendix C.

The fluence-dependent behavior of the ultrafast angular momentum transfer rate of Gd*T*$_2$Si$_2$ upon optical excitation is plotted in Fig. 7(d). While the angular momentum transfer rate increases with the normalized fluence, the systematic difference between the investigated compounds with GdRh$_2$Si$_2$ having the largest rate and GdCo$_2$Si$_2$ the smallest transfer rate remains consistent.

APPENDIX C: CORRECTION OF THE DEMAGNETIZATION AMPLITUDE CONSIDERING THE TRANSIENT PEAK SHIFT IN GdCo$_2$Si$_2$

Since the delay scans were acquired at constant momentum transfer Q, they may not reflect the correct antiferromagnetic order dynamics due to a transient peak shift in GdCo$_2$Si$_2$. In order to correct possible intensity modulation from the peak shift, we measured the transient evolution of the diffraction peak position of GdCo$_2$Si$_2$ at selected fluences and at selected delays [Fig. 8(a)]. The delay scans were acquired at the "shoulder" (the vertical dashed line) of the equilibrium peak to minimize such intensity variation. The diffraction peak intensity of GdCo$_2$Si$_2$ is modeled with a phenomenological Doniach-Sunjic function for precise description of the asymmetric peak shape,

$$DS(L; \alpha, \Gamma, Q, A) = A \left(\frac{\cos \frac{\pi \alpha}{2} + (1 - \alpha) \tan \frac{L - Q^{-1}}{\Gamma}}{[\Gamma^2 + (L - Q)^2]^{(1-\alpha)/2}} \right),$$
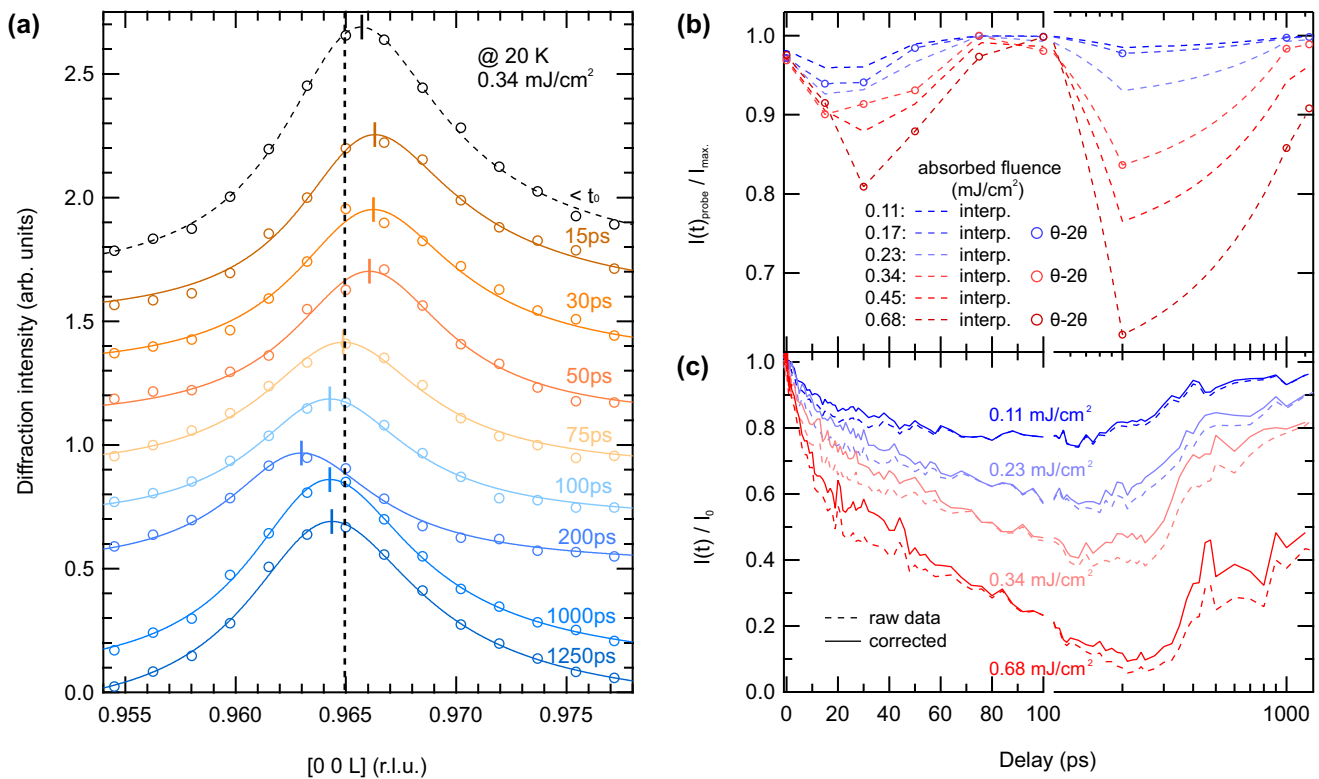
(C1)

FIG. 8. (a) Transient diffraction intensity evolution of the $(0\ 0\ q)$ reflection of GdCo$_2$Si$_2$ upon ultrafast optical excitation at selected delays. The vertical dashed line indicates the diffraction geometry for acquiring delay scans (see text). (b) The ratio between the intensity for probing the delay scan I_{probe} and the actual maximum intensity of the $(0\ 0\ q)$ diffraction intensity I_{max} at various pump fluences. Dashed lines indicate the linearly interpolated ratio based on the experimental data points. (c) The raw diffraction intensity dynamics (dashed lines) and the corrected diffraction intensity dynamics (solid lines) at various pump fluences.

where L is the position in reciprocal space $[0\ 0\ L]$. A is the amplitude of the peak, Q is the effective peak position, Γ is the effective peak width, and α determines the degree of asymmetry of the peak. For $\alpha = 0$, the equation becomes a symmetric Lorentzian profile, and asymmetry increases as α increases towards 1. The modeled intensity at the delay scan acquisition point I_{probe} (vertical dashed line) is clearly different from the modeled maximum intensity of the peak I_{max} for most pump-probe delays. The ratio between the two (I_{probe}/I_{max}) is plotted in Fig. 8(b). As we acquired the diffraction peak at selected delays, delay points in between the $\theta - 2\theta$ scans were linearly interpolated. Similarly, the fluence dependence in between measured fluences was linearly interpolated using the delay-interpolated ratio that was constructed in the previous step. The interpolated correction factors shown in Fig. 8(b) were applied to the raw delay scan intensity.

Figure 8(c) presents the corrected delay scans (solid lines) along with the raw delay scans (dashed lines) at selected fluences. As we see, the corrected intensity compensates the intensity loss from the transient peak shift at early and later phases of the dynamics.

APPENDIX D: ESTIMATION OF ABSORBED FLUENCE

All the reported fluences are total absorbed fluences, which were calculated using the measured incident fluences corrected for reflection and refraction effects. Calculation of absorbed fluence of GdRh$_2$Si$_2$ is reported in Ref. [11]. We

conducted reflectivity measurements of the other two samples using 1.55 eV light. We estimate the complex index of refraction at this photon energy as $n = n_0 + ik$; GdIr$_2$Si$_2$: $(2.97 \pm 0.18) + (2.52 \pm 0.25)i$; GdCo$_2Si_2$: $(4.64 \pm 0.46) + (3.77 \pm 0.68)i$. Using the indices of refraction, the total absorbed fluences were estimated. We estimate the penetration depth of 1.55 eV light to be 15.3 and 26.3 nm at the Bragg angle for GdCo$_2$Si$_2$ and GdIr$_2$Si$_2$, respectively.

APPENDIX E: ELECTRONIC STRUCTURE OF GdT_2Si$_2$

To elucidate the nature of the exchange coupling and observed magnetic properties in GdT_2Si$_2$ (T= Co 3*d*, Rh 4*d*, Ir 5*d*), the densities of states were calculated and analyzed (see Fig. 5). Gd 4*f* states are localized and located mostly 8 eV below the Fermi level. These states form localized magnetic moments which interact with each other via the itinerant conduction electrons (RKKY interaction). Since the spin polarization of the free electrons is crucial for the RKKY interaction, mainly Gd 5*d* and Si 3*p* states participate in the magnetic interaction. Si has an induced magnetic moment: 0.08 μ_B, 0.11 μ_B, 0.09 μ_B, for the cases with Co, Rh and Ir, respectively. Gd 5*d* electrons carry moments almost two times larger than Si 3*p*: 0.18 μ_B, 0.21 μ_B, 0.19 μ_B, respectively. It is remarkable that the conduction electrons are more spin polarized in GdRh$_2$Si$_2$ than in the other two compounds and this is in line with the strength of the calculated J's presented in the main text and observed Néel temperatures.

The *d* electrons of the transition metals are not spin polarized and therefore do not directly participate in the magnetic coupling. However, they are crucial for the covalent bonding in the compounds and are responsible for the formation of structural and electronic properties. Co *3d* states are strongly localized (mainly between 1 and 4 eV below the Fermi level). The localized nature of Co *3d* electrons in $GdCo_2Si_2$ is responsible for the significantly smaller unit cell volume than in $GdRh_2Si_2$ and $GdIr_2Si_2$: both *a* and *c* lattice parameters are about 5% smaller than in the other two compounds. Despite the smaller volume, Co *3d* states remain to be localized and hybridize less with Gd *5d* and Si *3p* states compared to Rh *4d* and Ir *5d* states. The latter two are more delocalized: The Rh *4d* and Ir *5d* bandwidth extends to the bottom of the valence zone at 6.7 and 7.6 eV below the Fermi level, respectively. From Fig. 5, one recognizes that Si *3p* and Gd *5d* electrons hybridize with the transition metal *d* orbitals only in the lower part of the valence zone: States below -2 eV belong mainly to d^{xz}, d^{3z^2-r}, and d^{yz} symmetries, while close to the Fermi level, the in-plane d^{xy}, $d^{x^2-y^2}$ symmetries dominate. In the case

of $GdCo_2Si_2$, Gd *5d* states with d^{xy} and $d^{x^2-y^2}$ symmetries are more dispersive since the in-plane lattice constant *a* is small and this leads to a stronger hybridization within the Gd layer. In the other two compounds, out-of-plane and in-plane Gd *5d* orbitals are clearly separated. This separation and a stronger localization of the orbitals result in a larger DOS at the Fermi level in $GdRh_2Si_2$ and $GdIr_2Si_2$, which increases the strength of the RKKY interaction. However, despite the more extended Ir *5d* orbitals, the DOS at the Fermi level is larger in $GdRh_2Si_2$ (and, thereby, the RKKY interaction is stronger). The main reason for this is the position of the transition metal antibonding *d* states above the Fermi level: in $GdRh_2Si_2$, they are located at 0.5 eV above the Fermi level, which is about 0.4 eV lower in energy than in $GdIr_2Si_2$. This leads to a stronger accumulation of the DOS at the Fermi level. In the case of $GdCo_2Si_2$, this argument does not hold since the strong in-plane hybridization of Gd *5d* electrons makes the states broader and reduces the DOS at the Fermi level, as discussed above.

[1] A. Aharoni, *Introduction to the Theory of Ferromagnetism* (Clarendon Press, Oxford, UK, 2000).

[2] J. Stöhr and H. C. Siegmann, *Magnetism* (Springer, Berlin, 2006).

[3] J. Jensen and A. R. Mackintosh, *Rare Earth Magnetism: Structures and Excitations*, The International Series of Monographs on Physics (Clarendon Press, Oxford, 1991).

[4] A. Vaterlaus, T. Beutler, and F. Meier, Spin-lattice relaxation time of ferromagnetic gadolinium determined with time-resolved spin-polarized photoemission, Phys. Rev. Lett. **67**, 3314 (1991).

[5] E. Beaurepaire, J.-C. Merle, A. Daunois, and J.-Y. Bigot, Ultrafast spin dynamics in ferromagnetic nickel, Phys. Rev. Lett. **76**, 4250 (1996).

[6] M. Wietstruk, A. Melnikov, C. Stamm, T. Kachel, N. Pontius, M. Sultan, C. Gahl, M. Weinelt, H. A. Dürr, and U. Bovensiepen, Hot-electron-driven enhancement of spin-lattice coupling in Gd and Tb 4*f* ferromagnets observed by femtosecond x-ray magnetic circular dichroism, Phys. Rev. Lett. **106**, 127401 (2011).

[7] B. Andres, M. Christ, C. Gahl, M. Wietstruk, M. Weinelt, and J. Kirschner, Separating exchange splitting from spin mixing in gadolinium by femtosecond laser excitation, Phys. Rev. Lett. **115**, 207404 (2015).

[8] B. Frietsch, J. Bowlan, R. Carley, M. Teichmann, S. Wienholdt, D. Hinzke, U. Nowak, K. Carva, P. M. Oppeneer, and M. Weinelt, Disparate ultrafast dynamics of itinerant and localized magnetic moments in gadolinium metal, Nat. Commun. **6**, 8262 (2015).

[9] L. Rettig, C. Dornes, N. Thielemann-Kühn, N. Pontius, H. Zabel, D. L. Schlagel, T. A. Lograsso, M. Chollet, A. Robert, M. Sikorski, S. Song, J. M. Glownia, C. Schüßler-Langeheine, S. L. Johnson, and U. Staub, Itinerant and localized magnetization dynamics in antiferromagnetic Ho, Phys. Rev. Lett. **116**, 257202 (2016).

[10] N. Thielemann-Kühn, D. Schick, N. Pontius, C. Trabant, R. Mitzner, K. Holldack, H. Zabel, A. Föhlisch, and C. Schüßler-

Langeheine, Ultrafast and energy-efficient quenching of spin order: Antiferromagnetism beats ferromagnetism, Phys. Rev. Lett. **119**, 197202 (2017).

[11] Y. W. Windsor, A. Ernst, K. Kummer, K. Kliemt, C. Schüßler-Langeheine, N. Pontius, U. Staub, E. V. Chulkov, C. Krellner, D. V. Vyalikh, and L. Rettig, Deterministic control of an antiferromagnetic spin arrangement using ultrafast optical excitation, Commun. Phys. **3**, 139 (2020).

[12] B. Frietsch, A. Donges, R. Carley, M. Teichmann, J. Bowlan, K. Döbrich, K. Carva, D. Legut, P. M. Oppeneer, U. Nowak, and M. Weinelt, The role of ultrafast magnon generation in the magnetization dynamics of rare-earth metals, Sci. Adv. **6**, eabb1601 (2020).

[13] B. Andres, S. E. Lee, and M. Weinelt, The role of spin-lattice coupling for ultrafast changes of the magnetic order in rare earth metals, Appl. Phys. Lett. **119**, 182404 (2021).

[14] Y. W. Windsor, S.-E. Lee, D. Zahn, V. Borisov, D. Thonig, K. Kliemt, A. Ernst, C. Schüßler-Langeheine, N. Pontius, U. Staub, C. Krellner, D. V. Vyalikh, O. Eriksson, and L. Rettig, Exchange scaling of ultrafast angular momentum transfer in 4*f* antiferromagnets, Nat. Mater. **21**, 514 (2022).

[15] K. Kliemt and C. Krellner, Single crystal growth and characterization of $GdRh_2Si_2$, J. Cryst. Growth **419**, 37 (2015).

[16] K. Kliemt, M. Peters, F. Feldmann, A. Kraiker, D.-M. Tran, S. Rongstock, J. Hellwig, S. Witt, M. Bolte, and C. Krellner, Crystal growth of materials with the $ThCr_2Si_2$ structure type, Cryst. Res. Technol. **55**, 1900116 (2020).

[17] G. Czjzek, V. Oestreich, H. Schmidt, K. Łąka, and K. Tomala, A study of compounds GdT_2Si_2 by Mössbauer spectroscopy and by bulk magnetization measurements, J. Magn. Magn. Mater. **79**, 42 (1989).

[18] L. D. Tung, J. J. M. Franse, K. H. J. Buschow, P. E. Brommer, and N. P. Thuy, A study of magnetic coupling in GdT_2Si_2 compounds (T = transition metal), J. Alloys Compd. **260**, 35 (1997).

[19] K. Kliemt, M. Hofmann-Kliemt, K. Kummer, F. Yakhou-Harris, C. Krellner, and C. Geibel, $GdRh_2Si_2$: An exemplary tetragonal

system for antiferromagnetic order with weak in-plane anisotropy, Phys. Rev. B **95**, 134403 (2017).

[20] U. Flechsig, F. Nolting, A. Fraile Rodríguez, J. Krempasky, C. Quitmann, T. Schmidt, S. Spielmann, and D. Zimoch, Performance measurements at the SLS SIM beam line, AIP Conf. Proc. **1234**, 319 (2010).

[21] N. B. Brookes, F. Yakhou-Harris, K. Kummer, A. Fondacaro, J. C. Cezar, D. Betto, E. Velez-Fort, A. Amorese, G. Ghiringhelli, L. Braicovich, R. Barrett, G. Berruyer, F. Cianciosi, L. Eybert, P. Marion, P. van der Linden, and L. Zhang, The beam line ID32 at the ESRF for soft x-ray high energy resolution resonant inelastic x-ray scattering and polarisation dependent x-ray absorption spectroscopy, Nucl. Instrum. Methods Phys. Res. Sect. A **903**, 175 (2018).

[22] K. Holldack, J. Bahrdt, A. Balzer, U. Bovensiepen, M. Brzhezinskaya, A. Erko, A. Eschenlohr, R. Follath, A. Firsov, W. Frentrup, L. Le Guyader, T. Kachel, P. Kuske, R. Mitzner, R. Müller, N. Pontius, T. Quast, I. Radu, J.-S. Schmidt, C. Schüßler-Langeheine *et al.*, FemtoSpeX: A versatile optical pump–soft x-ray probe facility with 100 fs x-ray pulses of variable polarization, J. Synchrotron Radiat. **21**, 1090 (2014).

[23] M. Geilhufe, S. Achilles, M. A. Köbis, M. Arnold, I. Mertig, W. Hergert, and A. Ernst, Numerical solution of the relativistic single-site scattering problem for the Coulomb and the Mathieu potential, J. Phys.: Condens. Matter **27**, 435202 (2015).

[24] M. Hoffmann, A. Ernst, W. Hergert, V. N. Antonov, W. A. Adeagbo, R. M. Geilhufe, and H. Ben Hamed, Magnetic and electronic properties of complex oxides from first-principles, Phys. Status Solidi B **257**, 1900671 (2020).

[25] J. P. Perdew, K. Burke, and M. Ernzerhof, Generalized gradient approximation made simple, Phys. Rev. Lett. **77**, 3865 (1996).

[26] V. I. Anisimov, J. Zaanen, and O. K. Andersen, Band theory and Mott insulators: Hubbard U instead of stoner I, Phys. Rev. B **44**, 943 (1991).

[27] A. I. Liechtenstein, M. I. Katsnelson, V. P. Antropov, and V. A. Gubanov, Local spin density functional approach to the theory of exchange interactions in ferromagnetic metals and alloys, J. Magn. Magn. Mater. **67**, 65 (1987).

[28] S. Tyablikov, *Methods in the Quantum Theory of Magnetism* (Plenum Press, New York, 1967).

[29] S.-E. Lee, Systematic study of the role of the indirect RKKY exchange interaction in ultrafast spin dynamics of 4*f* antiferromagnets, Ph.D. thesis, Freie Universität Berlin, 2023.

[30] I. D. Hughes, M. Dane, A. Ernst, W. Hergert, M. Luders, J. Poulter, J. B. Staunton, A. Svane, Z. Szotek, and W. M. Temmerman, Lanthanide contraction and magnetism in the heavy rare earth elements, Nature (London) **446**, 650 (2007).

[31] G. M. Müller, J. Walowski, M. Djordjevic, G.-X. Miao, A. Gupta, A. V. Ramos, K. Gehrke, V. Moshnyaga, K. Samwer, J. Schmalhorst, A. Thomas, A. Hütten, G. Reiss, J. S. Moodera, and M. Münzenberg, Spin polarization in half-metals probed by femtosecond spin excitation, Nat. Mater. **8**, 56 (2009).

[32] G. Salvatella, R. Gort, K. Bühlmann, S. Däster, A. Vaterlaus, and Y. Acremann, Ultrafast demagnetization by hot electrons: Diffusion or super-diffusion? Struct. Dyn. **3**, 055101 (2016).

[33] A. Fognini, T. U. Michlmayr, A. Vaterlaus, and Y. Acremann, Laser-induced ultrafast spin current pulses: A thermodynamic approach, J. Phys.: Condens. Matter **29**, 214002 (2017).

[34] S.-E. Lee, Y. W. Windsor, D. Zahn, A. Kraiker, K. Kummer, K. Kliemt, C. Krellner, C. Schüßler-Langeheine, N. Pontius, U. Staub, D. V. Vyalikh, A. Ernst, and L. Rettig, Dataset to: Controlling 4f antiferromagnetic dynamics via itinerant electronic susceptibility, Zenodo (2024).

[35] W. Rieger and E. Parthé, Ternary alkaline and rare earth silicides and germanides with $ThCr_2Si_2$ structure, Chem. Monthly **100**, 444 (1969).